

# Correlation effects in the ground state of trapped atomic Bose gases

Wirawan Purwanto\* and Shiwei Zhang†

*Department of Physics, The College of William and Mary, Williamsburg, Virginia 23187*

(Dated: April 18, 2018)

We study the effects of many-body correlations in trapped ultracold atomic Bose gases. We calculate the ground state of the gas using a ground-state auxiliary-field quantum Monte Carlo (QMC) method [Phys. Rev. E **70**, 056702 (2004)]. We examine the properties of the gas, such as the energetics, condensate fraction, real-space density, and momentum distribution, as a function of the number of particles and the scattering length. We find that the mean-field Gross-Pitaevskii (GP) approach gives qualitatively incorrect result of the kinetic energy as a function of the scattering length. We present detailed QMC data for the various quantities, and discuss the behavior of GP, modified GP, and the Bogoliubov method under a local density approximation.

## I. INTRODUCTION

The many-body physics in trapped Bose gases has drawn intense interest since the experimental realization of Bose-Einstein condensation (BEC) in ultracold, dilute alkali atoms [1]. The systems are “clean” and highly controllable experimentally. The dominant interactions are simple and well-understood, and the strength of the interatomic interactions can be readily tuned by means of Feshbach resonances [2]. With the recent realization of degenerate Fermi gases [3, 4, 5], these ultracold systems provide an ideal “laboratory” for studying many-body physics.

In the weakly-interacting regime, mean-field theories work quite well, for instance the Gross-Pitaevskii (GP) equation [6, 7, 8] for boson ground states. Much work has been done to study the ground state of the Bose atomic gases beyond mean field. For example, a modified GP equation was proposed [9] by inclusion of one-loop quantum corrections and the use of local-density approximation. Esry [10] developed a Hartree-Fock theory as a means of including the correlation effects in the BEC many-body calculations. Mazzanti and co-workers [11] applied a correlated basis theory [12] to study the detailed structure of dilute hard- and soft-sphere Bose gases. A comparative study for the modified GP and correlated basis approaches is presented in Ref. 13. Recently, McKinney and co-workers [14] used a many-body dimensional perturbation theory to compute the ground-state energy and breathing-mode frequency of spherically trapped gases at different interaction strengths.

Semianalytic methods are versatile and generally very easy to extend to realistic systems with large number of particles. However, they are approximate and each has its own limitations, especially in the strongly-interacting regime. Computational methods such as quantum Monte Carlo (QMC) provide a useful, complementary alternative. A variety of such calculations have been carried out for atomic boson systems, including variational Monte Carlo [15] and the exact diffusion Monte Carlo (DMC) [16, 17] studies on both the homogeneous [18] and trapped gases [19, 20, 21].

We have recently developed an auxiliary-field quantum

Monte Carlo (AF QMC) method [22] for the ground state of many-boson systems. While the standard DMC works in real space with particle configurations, our method works in the second-quantized formalism, which automatically accounts for particle permutation statistics. The calculation can be carried out in any single-particle basis. Conceptually, the method provides a way to systematically improve upon mean field while retaining its basic machinery, capturing correlation effects with a stochastic, coherent ensemble of independent-particle solutions. Various observables and correlation functions can be calculated relatively straightforwardly.

The initial motivation of this study was to use the AF QMC method to quantify, by direct comparison with GP, the effects of interactions in trapped Bose gases, and to provide additional precise numerical data where they were not available. (Although the method is not exact for bosons with repulsive interactions, the systematic errors are very small in the parameter region of interest, as we show below.) In particular, we were interested in the behavior of the system as a function of the interaction strength, which, unlike in typical condensed matter systems, can be probed directly in experiments. We found that GP yielded significant errors in the energetics in the Feshbach resonance regime, which resulted in a qualitatively incorrect behavior of the kinetic energy in GP as a function of the scattering length. To study the origin of these errors, we carried out additional calculations using first-order Bogoliubov results under a local-density approximation (LDA). The purpose of this paper is thus to present our QMC data, and discuss the behavior of the GP, modified GP, and Bogoliubov-LDA methods as benchmarked by QMC.

The rest of the paper is organized as follows. In Sec. II, we describe the many-body Hamiltonian. Our QMC method is summarized in Sec. III, as are the procedures of our GP and Bogoliubov-LDA calculations. Results from QMC, GP, and first-order Bogoliubov-LDA methods are presented in Sec. IV, where we study the energetics of the gas in three dimensions as a function of the number of particle  $N$  and the  $s$ -wave scattering length  $a_s$ , and examine the density profile and momentum distribution. Our study extends to the strongly-interacting regime achievable by Feshbach resonances. In Sec. V, we discuss the implications of our comparisons between GP, modified GP, Bogoliubov-LDA and QMC. In addition, we also discuss the influence of the details of the two-body potential. Concluding remarks are given in Sec. VI. Finally, in the appendix, we describe additional details on our

\*Electronic address: wirawan@camelot.physics.wm.edu

†Electronic address: shiwei@physics.wm.edu

Bogoliubov and QMC calculations, including benchmark results on the systematic errors in our QMC.

## II. MODIFIED BOSE-HUBBARD MODEL

We consider  $N$  Bose particles in a three-dimensional cube of side length  $2r_b$ , under the periodic boundary condition. Similar to our earlier work [22], we use the Bose-Hubbard model as the discrete representation of the many-body Hamiltonian on a real-space lattice:

$$\begin{aligned} \hat{H} &= \frac{\hbar^2}{2m} \sum_{\mathbf{k}} k^2 \hat{\varphi}^\dagger(\mathbf{k}) \hat{\varphi}(\mathbf{k}) \\ &+ \frac{1}{2} m \omega_0^2 \int d^3 \mathbf{r} r^2 \hat{\psi}^\dagger(\mathbf{r}) \hat{\psi}(\mathbf{r}) \\ &+ \frac{1}{2} \left( \frac{4\pi a_s \hbar^2}{m} \right) \\ &\times \int d^3 \mathbf{r}_1 \int d^3 \mathbf{r}_2 \hat{\psi}^\dagger(\mathbf{r}_1) \hat{\psi}^\dagger(\mathbf{r}_2) \delta(\mathbf{r}_1 - \mathbf{r}_2) \hat{\psi}(\mathbf{r}_2) \hat{\psi}(\mathbf{r}_1), \end{aligned} \quad (1)$$

where the kinetic energy operator is modified from the Bose-Hubbard form we used earlier, and is expressed in momentum space instead, with

$$\hat{\varphi}(\mathbf{k}) = \frac{1}{(2r_b)^{3/2}} \int d\mathbf{r} \hat{\psi}(\mathbf{r}) e^{i\mathbf{k}\cdot\mathbf{r}}. \quad (2)$$

The sum over  $\mathbf{k}$  is taken over all the (discretized) momentum coordinates. Equation (1) describes both the homogenous and trapped Bose gases. For a homogenous gas,  $\omega_0 = 0$ . In both cases, we use a large enough  $r_b$  to minimize the boundary effects. We will set  $\hbar = m = 1$  throughout this paper.

We discretize the cubic simulation box into an  $L \times L \times L$  lattice. The lattice spacing is  $\varsigma = 2r_b/L$ . We enumerate the real-space sites using an integral index  $i$  ranging from 1 through  $L^3$ . The coordinate of the  $i$ -th site is given by  $\mathbf{r}_i$ . The periodic boundary condition restricts the values for the momentum coordinates  $\mathbf{k} = (k_1, \dots, k_3)$  to  $k_i = \pi n_i / r_b$ , where  $n_i$  is an integer in the range  $[-L/2] \leq n_i < [L/2]$ . We will use the index  $q = 1, 2, \dots, L^3$  to enumerate the points in the momentum space; correspondingly,  $\mathbf{k}_q$  is the momentum vector of the  $q$ -th point.

The field operators on the lattice are defined to be

$$c_i \equiv \varsigma^{3/2} \hat{\psi}(\mathbf{r}_i), \quad (3)$$

$$b_q \equiv \hat{\varphi}(\mathbf{k}_q). \quad (4)$$

The discretized Hamiltonian is therefore given by

$$\begin{aligned} \hat{H} &= \frac{1}{2} \sum_q \mathbf{k}_q^2 b_q^\dagger b_q + \frac{1}{2} \left( \frac{\kappa}{\varsigma^2} \right) \sum_i |\mathbf{r}_i - \mathbf{r}_0|^2 c_i^\dagger c_i \\ &+ \frac{1}{2} U \sum_i \left( c_i^\dagger c_i c_i^\dagger c_i - c_i^\dagger c_i \right), \end{aligned} \quad (5)$$

where

$$U = \frac{4\pi a_s}{\varsigma^3}, \quad (6)$$

$$\kappa = \frac{\varsigma^2}{a_{\text{ho}}^4}, \quad (7)$$

and  $a_{\text{ho}} \equiv \sqrt{\hbar/m\omega_0}$  is the harmonic oscillator length scale. The representation of the kinetic energy in Eq. (5) reproduces the continuum spectrum more faithfully than the real-space finite-difference form in the original Hubbard form, and allows quicker convergence with the size of the grid,  $L$ .

The contact two-body potential in the continuum is ill-defined [23, 24] because of the ultraviolet divergence. The momentum-space interaction strength,

$$\tilde{V}_{2B}(\mathbf{q}) \equiv \int d\mathbf{r} V_{2B}(\mathbf{r}) e^{-i\mathbf{q}\cdot\mathbf{r}},$$

is uniform for any  $|\mathbf{q}|$ . The discretized Hamiltonian alleviates the problem to a large degree by introducing a momentum space cut-off  $k_c$  and replacing the  $\delta$ -potential by an on-site interaction parameterized by the scattering length,  $a_s$ . However, the discretized two-body potential in Eq. (5) must be adjusted in order to yield the correct two-body scattering length, and  $a_s$  in Eq. (6) must be replaced by an appropriate  $a'_s$  for the lattice. Following the standard treatment, we obtain the regularized  $a'_s$ , which for a 3D lattice is [25]

$$a'_s \equiv \frac{a_s}{1 - 2.442749 a_s / \varsigma}. \quad (8)$$

For the system to be in the dilute limit and the form of our two-body potential to be valid, we need the density at the lattice sites to satisfy  $\langle \hat{n}_i \rangle \ll 1$ .

## III. COMPUTATIONAL METHODS

### A. Quantum Monte Carlo method

#### 1. General formalism for many-boson ground states

We briefly describe our method of computing the ground state of many bosons. A detailed account can be found in Ref. 22. We project the ground-state wave function  $|\Phi_0\rangle$  from a trial wave function  $|\Psi_T\rangle$ ,

$$(\mathcal{P}_{\text{gs}})^n |\Psi_T\rangle \xrightarrow{n \rightarrow \infty} |\Phi_0\rangle, \quad (9)$$

where  $|\Psi_T\rangle$  in this study is the GP solution (see Sec. III B for details). The projector

$$\mathcal{P}_{\text{gs}} \equiv e^{\Delta\tau E_T} e^{-\Delta\tau \hat{H}} \quad (10)$$

$$= e^{\Delta\tau E_T} e^{-\frac{1}{2}\Delta\tau \hat{K}} e^{-\Delta\tau \hat{V}} e^{-\frac{1}{2}\Delta\tau \hat{K}} + \mathcal{O}(\Delta\tau^2) \quad (11)$$

is evaluated stochastically by rewriting the two-body part into a multidimensional integral.

The two-body part of the potential in Eq. (5) can be written as a sum of the squares of one-body operators  $\hat{V} = -\frac{1}{2} \sum_i \hat{v}_i^2$ , where  $\hat{v}_i \equiv \sqrt{-U} c_i^\dagger c_i$  is essentially the density operator. We use the following Gaussian integral identity to rewrite  $e^{-\Delta\tau \hat{V}}$  in terms of the one-body operators:

$$e^{\frac{1}{2}\Delta\tau \hat{v}^2} = \frac{1}{\sqrt{2\pi}} \int_{-\infty}^{\infty} d\sigma e^{-\frac{1}{2}\sigma^2} e^{\sigma\hat{v} - \frac{1}{2}\sigma^2} e^{\sqrt{\Delta\tau}(\sigma - \bar{\sigma})\hat{v}}, \quad (12)$$

where the constant  $\bar{\sigma}$  is determined below. We use an importance sampling scheme to sample the ground-state wave function, so that

$$|\Phi_0\rangle \doteq \sum_{\{\phi\}} w_\phi \frac{|\phi\rangle}{\langle \Psi_T | \phi \rangle}, \quad (13)$$

where each  $|\phi\rangle$  is a mean-field solution, i.e., a permanent consisting of identical single-particle orbitals. In practice, this means that each  $|\phi\rangle$  is represented by a single-particle orbital.

The projection in Eq. (9) is then realized by random walks in a manifold of mean-field solutions [22, 26], which are governed by the following equation [22, 27]:

$$|\phi'\rangle = \int d\sigma p(\sigma) \hat{B}(\sigma - \bar{\sigma}) W(\sigma, \phi) |\phi\rangle, \quad (14)$$

where

$$p(\sigma) = \prod_i \frac{e^{-\frac{1}{2}\sigma_i^2}}{\sqrt{2\pi}}, \quad (15)$$

$$\hat{B}(\sigma - \bar{\sigma}) = e^{\Delta\tau E_T} e^{-\frac{1}{2}\Delta\tau \hat{K}} \left\{ \prod_i e^{\sqrt{\Delta\tau}(\sigma_i - \bar{\sigma}_i)\hat{v}_i} \right\} \times e^{-\frac{1}{2}\Delta\tau \hat{K}}, \quad (16)$$

$$W(\sigma, \phi) = \frac{\langle \Psi_T | \hat{B}(\sigma - \bar{\sigma}) |\phi\rangle}{\langle \Psi_T | \phi \rangle} e^{\sigma \cdot \bar{\sigma} - \frac{1}{2}\bar{\sigma} \cdot \bar{\sigma}}. \quad (17)$$

The optimal choice of the constant vector  $\bar{\sigma}$  is [22, 27]:

$$\bar{\sigma}_i = -\sqrt{\Delta\tau} \frac{\langle \Psi_T | \hat{v}_i | \phi \rangle}{\langle \Psi_T | \phi \rangle} \equiv -\sqrt{\Delta\tau} \bar{v}_i. \quad (18)$$

With this choice, the weight factor in Eq. (14) can be written in the so-called local energy form [22, 27]:

$$W(\sigma, \phi) \approx e^{-\Delta\tau \langle \Psi_T | \hat{H} | \phi \rangle / \langle \Psi_T | \phi \rangle} \equiv e^{-\Delta\tau E_L(\phi)}. \quad (19)$$

In practice, whether the local-energy or the hybrid form in Eq. (17) is more efficient will depend on the system. For the calculations in this paper, we have mostly used the local-energy form.

We initialize a population  $\{|\phi\rangle\}$  to mean-field solutions, e.g.,  $|\Psi_T\rangle$ . A single random-walk step for each walker consists of updating the orbital and its associated weight  $w_\phi$ ,

$$|\phi'\rangle \leftarrow \hat{B}(\sigma - \bar{\sigma}) |\phi\rangle \quad (20a)$$

$$w_{\phi'} \leftarrow W(\sigma, \phi) w_\phi. \quad (20b)$$

where the auxiliary fields  $\{\sigma_i\}$  are drawn from the Gaussian probability density function  $p(\sigma)$ .

The computation of observables is done using the back-propagation estimator [22, 26],

$$\hat{A}_{\text{bp}} = \frac{\langle \Psi_T | e^{-\tau_{\text{bp}} \hat{H}} \hat{A} | \Phi_0 \rangle}{\langle \Psi_T | e^{-\tau_{\text{bp}} \hat{H}} | \Phi_0 \rangle}, \quad (21)$$

which for large enough  $\tau_{\text{bp}}$  yields the ground-state expectation value for any observable.

## 2. Phaseless approximation

The formalism above is exact. For repulsive interactions, unfortunately,  $\hat{v}_i$  in Eq. (12) becomes imaginary. This is similar to the phase problem in fermionic systems [27], and we apply the recently developed *phaseless approximation*, which has been shown to work well in electronic-structure calculations [27]. This method eliminates the phase problem at the cost of a systematic bias which is dependent on the trial wave function. As we will demonstrate in benchmark calculations in Appendix A, the bias is relatively small for the bosonic systems we study here. Indeed, for all but the largest values of  $a_s$ , it is possible to perform unconstrained calculations with fixed imaginary-time,  $\beta = n\Delta\tau$ , in which  $\beta$  can be made sufficiently long that essentially exact ground-state values are obtained. Comparison with these results shows that the systematic error in the phaseless approximation is small (see Appendix A).

In the phaseless approximation, the weights  $\{w_\phi\}$  are restricted to real, positive values. We define the phase rotation angle  $\Delta\theta$  by

$$\Delta\theta \equiv \Im \ln \left( \frac{\langle \Psi_T | \phi' \rangle}{\langle \Psi_T | \phi \rangle} \right). \quad (22)$$

This is the complex-phase rotation of the walker's overlap with the trial wave function as a result of the application of  $\hat{B}(\sigma - \bar{\sigma})$  to  $|\phi\rangle$ . In the phaseless approximation, the evolution of  $w_\phi$  is altered to

$$w_{\phi'} \leftarrow \begin{cases} \cos(\Delta\theta) |W(\sigma, \phi)| w_\phi, & |\Delta\theta| < \pi/2 \\ 0, & \text{otherwise} \end{cases}, \quad (23)$$

which prevents the walkers from reaching the origin of the  $\langle \Psi_T | \phi \rangle$ -complex-plane. Equations (20a) and (23) define the algorithm of the phaseless QMC method.

In invoking the phaseless approximation, it is helpful to rearrange the two-body interaction term in  $\hat{H}$  such that a mean-field background is subtracted:

$$\hat{V} = -\frac{1}{2} \sum_i (\hat{v}_i - \langle \hat{v}_i \rangle)^2 - \sum_i \hat{v}_i \langle \hat{v}_i \rangle + \frac{1}{2} \sum_i \langle \hat{v}_i \rangle^2, \quad (24)$$

where the constant  $\langle \hat{v}_i \rangle$  is the mean-field expectation value, e.g., with respect to  $|\Psi_T\rangle$ . The residual term involving

$(\hat{v}_i - \langle \hat{v}_i \rangle)$  is then used in Eq. (12). This would have *no effect* in the exact formalism above, where, as we discussed in Ref. 22, the importance sampling transformation effectively introduces the background subtraction even if the bare form of  $\hat{V}$  is used. With the phaseless approximation, however, the rotation angle is controlled by the mixed-estimate of  $\hat{v}_i$ . Reducing its average by subtracting the mean-field background will thus help reduce the rotation, and improve the behavior of the approximation in Eq. (23).

We note that the presence of phaseless approximation breaks the time-reversal symmetry of the ground-state projector. The forward, phaseless propagator  $(e^{-\tau_{\text{bp}} \hat{H}})_{\text{ph}}$  is no longer formally equivalent to the back-propagated, phaseless propagator  $(e^{-\tau_{\text{bp}} \hat{H}})_{\text{ph}}^\dagger$  [see Eq. (21)]. This results in an additional systematic error in the back-propagation estimator. The expectation value of an operator  $\hat{A}$  computed from back-propagation is  $\langle \Phi_0'' | \hat{A} | \Phi_0' \rangle$ , where  $|\Phi_0'\rangle$  and  $|\Phi_0''\rangle$  are the approximate ground-state wave functions (normalized) in the forward- and backward-direction, respectively, and they are in general not the same. This is similarly the case in the constrained-path Monte Carlo for fermion lattice models [26, 28]. It was shown [28] that the error vanishes linearly as  $|\Psi_T\rangle \rightarrow |\Phi_0\rangle$ . We will further discuss the effect of the phaseless constraint in Sec. V and Appendix A.

## B. GP self-consistent projection and QMC trial wave functions

We solve the GP equation on the same lattice defined for QMC, using a self-consistent projection with the GP propagator  $\exp(-\Delta\tau \hat{H}_{\text{GP}})$  [22]. Aside from a factor  $(N-1)/N$  in front of the interaction terms, the one-body Hamiltonian  $\hat{H}_{\text{GP}}$  is simply Eq. (5) with the replacement

$$c_i^\dagger c_i^\dagger c_i c_i \rightarrow 2\langle c_i^\dagger c_i \rangle c_i^\dagger c_i - \langle c_i^\dagger c_i \rangle^2, \quad (25)$$

where the expectation is with respect to the GP solution. As discussed in Ref. 22, our QMC can be thought of as stochastically carrying out the functional integral, while GP is the saddle-point approximation.

The  $U$  parameter in the GP calculations is given by the bare  $a_s$  rather than the regularized  $a'_s$  using Eq. (8), because the shape-independent  $\delta$  potential has become a mean-field potential in the GP approximation. It is these GP results that we compare with.

For our QMC calculations, the trial wave function  $\Psi_T$  is taken to be the solution of the GP-like projection, but with the regularized  $a'_s$ . This wave function is different from the correct GP solution above, which is obtained using the bare  $a_s$ . Each value of the discretization parameter  $\varsigma$  corresponds to a different renormalized  $a'_s$  [see Eq. (8)], and gives rise to distinctly different results, while the correct GP solution converges rapidly with  $\varsigma$  (see Fig. 8). As the trial wave function, however, we argue that the optimal choice is the best variational solution, which is given by the corresponding mean-field calculation with the same  $a'_s$ .

## C. Bogoliubov approximation

In the Bogoliubov approximation [29, 30, 31], correlation effects are treated by means of perturbation, where the zeroth-order term is the GP mean-field solution. The approach was first formulated for a homogenous Bose gas. It assumes a macroscopic occupancy of the lowest energy state ( $\mathbf{k} = \mathbf{0}$ ), namely  $(N - N_0) \ll N$ . For each density  $\rho = N/\Omega$  and interaction strength, the total energy per particle  $E_{\text{Bog}}/N$ , momentum distribution  $\pi_{\text{Bog}}(\mathbf{k})$ , and condensate fraction  $N_0/N$  can be written down analytically in the thermodynamic limit. The corrections to the mean-field GP results are expressed in terms of the gas parameter  $\rho a_s^3$ , which gives a measure of the deviation from the mean-field picture. Note that the bare  $a_s$  should be used, since the regularization of the scattering length is implicitly done in the Bogoliubov approximation as is in GP.

It is important to truncate the summation over  $\mathbf{k}$  in computing the momentum distribution and kinetic energy. This stems from the incorrect behavior of the Bogoliubov  $\pi(\mathbf{k})$  at large momenta:  $\pi_{\text{Bog}}(\mathbf{k}) \propto 1/|\mathbf{k}|^4$  as  $|\mathbf{k}| \rightarrow \infty$ . Physically, the form of the two-body potential requires that  $|\mathbf{k}|a_s \ll 1$ , therefore the contribution from  $|\mathbf{k}|$  larger than a cutoff momentum  $k_c$  should be excluded. We use an explicit numerical summation with the same  $\mathbf{k}$ -space grid as in QMC. This automatically limits the sum to the reciprocal lattice (excluding  $\mathbf{k} = \mathbf{0}$ ). In addition, it helps to correlate the finite-size effects in the two calculations, and allows for a more direct comparison of the results between Bogoliubov and QMC.

We extend the Bogoliubov approach to the inhomogeneous case using a local-density approximation (LDA), by treating each lattice site as a locally homogenous Bose gas. This is similar to the LDA approximation for electronic systems under density functional theory [32], and we refer to it as *Bogoliubov-LDA*. The approximation is expected to be reasonable if the density is smooth and slowly varying, which is fulfilled in our dilute Bose gas systems.

The kinetic energy, for example, is a sum of two contributions under this approach: one from the curvature (inhomogeneity) of the density profile, and the other from Bogoliubov correction. Given the real-space density  $\rho(\mathbf{r})$ , it is

$$\begin{aligned} \langle \hat{T} \rangle_{\text{Bog-LDA}} &= -\frac{1}{2} \int d^3\mathbf{r} \sqrt{\rho(\mathbf{r})} \nabla^2 \sqrt{\rho(\mathbf{r})} \\ &+ \int d^3\mathbf{r} \tilde{T}_{\text{Bog}}[\rho(\mathbf{r})] \rho(\mathbf{r}), \end{aligned} \quad (26)$$

where the functional  $\tilde{T}_{\text{Bog}}[\rho(\mathbf{r})]$  is the Bogoliubov kinetic energy per particle for a gas with uniform density  $\rho = \rho(\mathbf{r})$ . More details on our Bogoliubov-LDA procedure are provided in Appendix B.)

## IV. RESULTS

In this section, we present results on the energetics, condensate fraction, density profile, and momentum distribution. Individual energy terms are computed:  $\langle \hat{T} \rangle$  is the kinetic en-



ergy,  $\langle \hat{V}_{2B} \rangle$  the two-body interaction energy, and  $\langle \hat{V}_{\text{trap}} \rangle$  the external trapping potential.

In the calculations, we typically use a  $24 \times 24 \times 24$  lattice, with a simulation box of linear dimension  $2r_b = 14a_{\text{ho}}$ . This gives us a lattice constant of  $\zeta = 0.583a_{\text{ho}}$ . Our trap length is  $a_{\text{ho}} = 8546 \text{ \AA}$ , which gives typical peak densities of about 10 to  $40 \mu\text{m}^{-3}$  for 100 to 1000 particles in the trap. The lattice constant  $\zeta$  is large compared to our scattering lengths (up to  $a_s \sim 1000 \text{ \AA}$ ), which is consistent with the assumption in neglecting the details of the two-body potential.

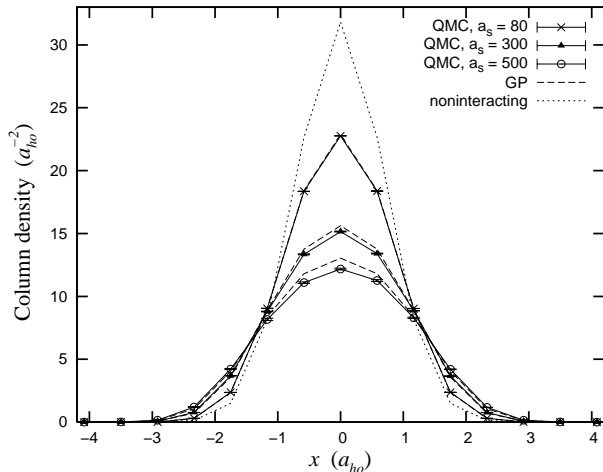


FIG. 1: The ground-state column density  $\rho_y(x, z=0)$  of a trapped gas containing  $N = 100$  bosons with three different scattering lengths:  $a_s = 80 \text{ \AA}$ ,  $300 \text{ \AA}$ , and  $500 \text{ \AA}$ . QMC statistical error bars are indicated. The GP densities are next to the corresponding QMC curve, and are all shown in dashed lines. Also shown as a reference is the non-interacting profile.

### A. Density Profile

Figure 1 shows the density profiles of 100 trapped bosons for three different scattering lengths. To make a connection with experiments, we show the column density

$$\rho_y(x, z) \equiv \int dy \rho(x, y, z), \quad (27)$$

that is, the density integrated along a particular direction (e.g., the  $y$ -axis), which can be observed through optical measurements [33, 34, 35]. As we increase  $a_s$ , the condensate expands due to the increasing repulsive interactions. Similarly, as we add more particles into the gas, the density profiles expands, as shown in Fig. 2.

Compared to GP, the QMC peak density is always lowered, and the QMC overall density profile is more extended. For  $a_s = 80 \text{ \AA}$ , the peak column density is lowered by 0.5% from GP. For  $a_s = 500 \text{ \AA}$ , this difference is about 7%. Earlier many-body calculations using the correlated basis approach [13, 36] and DMC [19, 21] also showed the same qualitative behavior. Below we will further discuss these in connection with the energetics and momentum distribution.

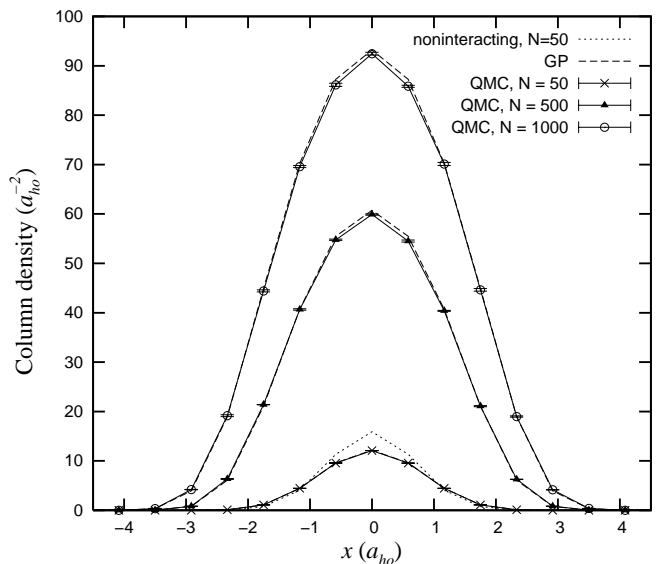


FIG. 2: The ground-state column density  $\rho_y(x, z=0)$  of a trapped gas of  $N = 50-1000$  bosons with scattering length of  $a_s = 120 \text{ \AA}$ .

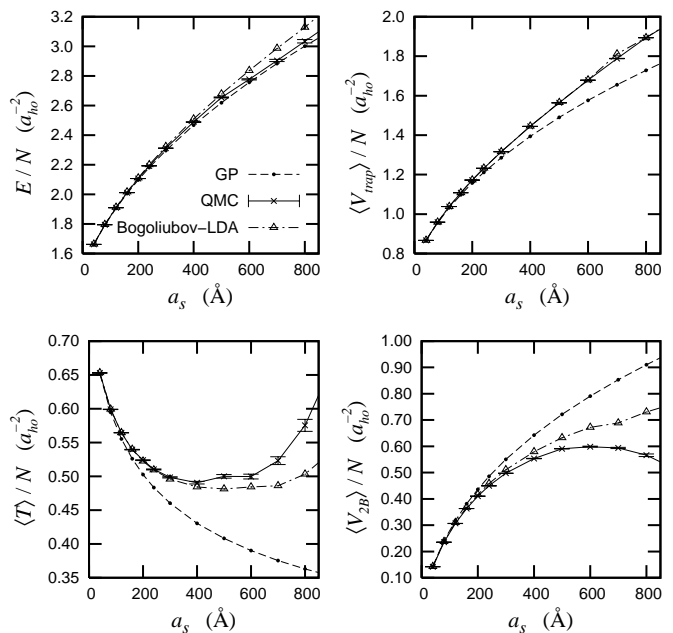


FIG. 3: Ground-state energy per particle and its individual components as a function of the scattering length. The system has 100 bosons. QMC error bars are statistical.

### B. Energetics

Figure 3 shows the ground-state energy and its individual components as a function of the interaction strength. We see that, as the scattering length  $a_s$  is increased, the total energy increases as expected. Both GP and Bogoliubov-LDA energies are in reasonable agreement with QMC, deviating more at larger  $a_s$ . The GP energy is slightly lower than the exact

results (no variational principle due to regularization), while Bogoliubov-LDA is higher. The external potential energy,  $\langle \hat{V}_{\text{trap}} \rangle$ , also increases with  $a_s$ , which is a consequence of the expansion of the density profile with interaction, as shown in Fig. 1. The GP trap energy is lower than QMC, consistent with the result in Fig. 1 that QMC density profiles are more extended.

The kinetic and interaction energies are shown in the bottom panels of Fig. 3. The discrepancy between GP and QMC is more pronounced. In particular, the GP kinetic energy decreases monotonically with  $a_s$ , because the density profile expands and the system becomes less confined. The QMC kinetic energy, on the other hand, shows a *nonmonotonic behavior*. For small  $a_s$ , the kinetic energy decreases as  $a_s$  is increased, tracking the GP result. At  $a_s \gtrsim 400$  Å, however, the kinetic energy curves up and increases with  $a_s$ . The QMC interaction energy is significantly lower than the mean-field interaction energy at large  $a_s$ , and the GP result increases much more rapidly with  $a_s$  than QMC. Indeed the QMC curve appears to turn downward at the last point, but our data is not sufficient to establish this, as it is possible that a larger systematic error from the phaseless approximation may have contributed to make the QMC result smaller (see the benchmark results in Appendix A).

From a single-particle picture, we would expect the QMC kinetic energy to be lower than that of GP, since the QMC density profiles are more extended. In reality, correlation effects become more important as  $a_s$  increases, which raises the kinetic energy with interaction. This is illustrated clearly by considering the uniform Bose gas, for which we show corresponding results in Fig. 4. The GP ground state is a zero-momentum condensate. In the many-body ground state, interactions excite particles into higher-momentum single-particle states, raising the kinetic energy as a result. The QMC results

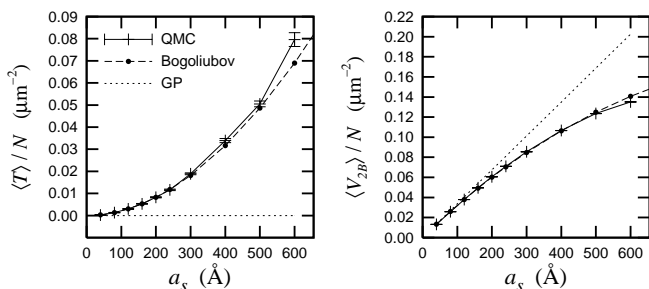


FIG. 4: Kinetic and interaction energies in the *uniform Bose gas* as a function of the scattering length. We show results from QMC, Bogoliubov, and GP. The density is  $\rho = 0.542 \mu\text{m}^{-3}$ . The simulation box has 100 particles on a  $16 \times 16 \times 16$  lattice, representing a physical volume of  $\Omega = 184.4 \mu\text{m}^3$ .

in the trapped gas are thus the outcome of the competition between mean-field and correlation effects.

The Bogoliubov-LDA calculations, whose results are also shown in Fig. 3, help to quantify this picture further. We use QMC density profiles in the calculation (hence the exact agreement between the Bogoliubov-LDA and QMC estimates of the trap energy in Fig. 3), although we have verified that the

physics is qualitatively unchanged if the GP densities are used instead. The result shows good agreement with the full many-body calculation. In particular, the Bogoliubov kinetic energy shows an increase similar to the QMC prediction. The corresponding interaction energy is also reduced, although not as much as in QMC. Overall, the Bogoliubov results capture the basic picture and confirm that correlations are an important ingredient in the energetics of the gas.

### C. Condensate fraction and momentum distribution

Figure 5 shows the condensate fraction as a function of interaction strength. GP by definition gives 100%. We see that the actual depletion is about 4% at 800 Å. Again, the Bogoliubov result agrees well with QMC. Figure 6 shows the mo-

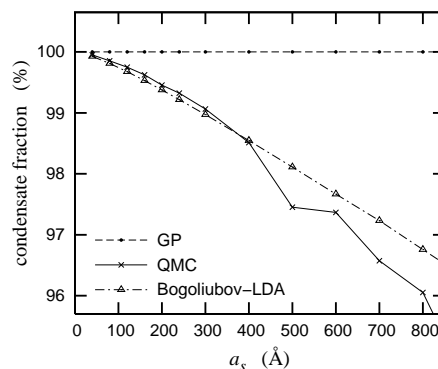


FIG. 5: Condensate fraction as a function of the scattering length. The system is the same as that of Fig. 3. The condensate fraction is defined as the leading eigenvalue (normalized by  $N$ ) of the one-body real-space density matrix. QMC statistical errors were not shown.

mentum distribution for two scattering lengths:  $a_s = 200$  Å and  $500$  Å. The QMC's momentum distribution is more peaked than GP. This translates in the real space to a more extended density profile for QMC, as is observed in Fig. 1.

The graph also shows the contribution to the kinetic energy from various  $k \equiv |\mathbf{k}|$  regions, since the kinetic energy is related to the momentum distribution through

$$\langle \hat{T} \rangle \propto \int k^2 dk \pi(k) k^2. \quad (28)$$

Relative to GP, the QMC distribution is depleted in the medium- $k$  regime, around  $k \sim a_{\text{ho}}^{-1}$ . Part of this depletion goes to the low-momentum region near  $k = 0$ , and the other to the high- $k$  region. At a higher  $a_s$ , the depletion shifts toward the smaller  $k$  region. It is clear that the enhancement in the high- $k$  region results in the increase of the kinetic energy. The kinetic energy is strongly enhanced in the larger  $a_s$  cases, which results in the upturn of the kinetic energy curve in Fig. 3.

A precision measurement of the momentum distribution would be useful to reveal the detailed structure of the many-body correlations in the Bose gas. Our results from a lattice do not have enough resolution to reveal whether there are finer

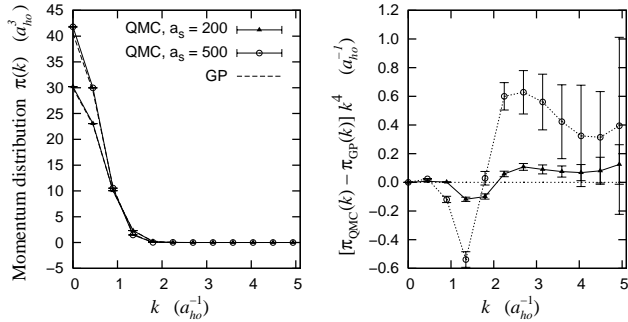


FIG. 6: Momentum distribution for trapped gases at two different scattering lengths. The system again has  $N = 100$  bosons. The left panel shows a cut along the  $k$ -axis. The right panel shows the difference between the QMC and GP, multiplied by  $k^4$ .

structures in the momentum- or real-space density. (A fine structure in the density profile was predicted by the DMC calculations [21].) In the auxiliary-field QMC framework, a better resolution in the density profile may be obtained by choosing a more suitable basis set, such as Hartree-Fock states [10], whereby the GP solution becomes the lowest-energy state in this basis set, and also the leading solution in the ground-state wave function.

## V. DISCUSSIONS

### A. GP, modified GP, and Bogoliubov-LDA approaches

We have shown that the many-body correlations qualitatively change the behavior of the kinetic energy in the trapped Bose gas. The Bogoliubov approximation [29, 30, 31] under the local density approximation (LDA), which we refer to as Bogoliubov-LDA, captures this trend quite well. The LDA provides a good way to include the correlation effects based on the homogenous Bose gas results. This is perhaps not surprising, given the diluteness of the gas.

In contrast, the mean-field GP method by construction approximates the kinetic energy only by the part that arises from the inhomogeneity of the gas, missing the portion from many-body effects. The separation of these two portions is especially clear in the homogeneous gas, as we illustrated in Sec. IV B. This appears to be a rather generic feature of independent-particle approaches. The same would apply to the modified GP (MGP) method [9, 13, 37, 38, 39], which can be viewed as the bosonic counterpart of the standard electronic structure method of LDA under density-functional theory (DFT). In that framework, the MGP equation is an outcome of using the Bogoliubov results for the uniform Bose gas as the “exchange-correlation” (xc) functional, i.e., LDA+Bogoliubov (*as opposed to* the Bogoliubov-LDA above). This method has a great advantage in that it allows self-consistent calculations. For example, the real-space density can be calculated directly and would not need to be imported as was done with the Bogoliubov-LDA. Further, it is of course possible to use exact QMC results on the uniform gas

to further improve the MGP equation, and make it more like DFT-LDA. For the kinetic energy, however, the MGP would give the same qualitative results as GP, even when the exact xc-functional is used and the exact density is obtained, because the “kinetic energy” that is explicitly defined in the MGP framework is incomplete. In fact, the same would seem to apply to DFT-LDA for electronic systems. This is an important conceptual difference between MGP and Bogoliubov-LDA approach, although they are closely related and lead to the same total energy results.

### B. Finite-size effects and limitations of the on-site potential

There are two kinds of finite-size errors in our calculation: the error due to finite simulation box size, and the discretization error due to finite lattice constant. The first kind is easily reduced, by increasing the simulation box size,  $r_b$ . In the trapped boson calculations with  $N = 100$  particles, we have checked that  $r_b \gtrsim 5a_{ho}$  is sufficient for  $a_s \leq 1000$ . For calculations with large values of  $N$ , we use  $r_b = 7a_{ho}$  to allow simulations of large enough condensate while keeping the finite-size errors much less than our statistical error.

The discretization error from the finite lattice constant,  $\varsigma$ , is more subtle. On the one hand, sufficiently small  $\varsigma$  should be used so the results converge to the continuum values. Figure 7 shows the convergence of the total energy. It also illustrates the effect of regularizing the scattering length, as discussed in Sec. II. In Fig. 8, we show the convergence of the density profile.

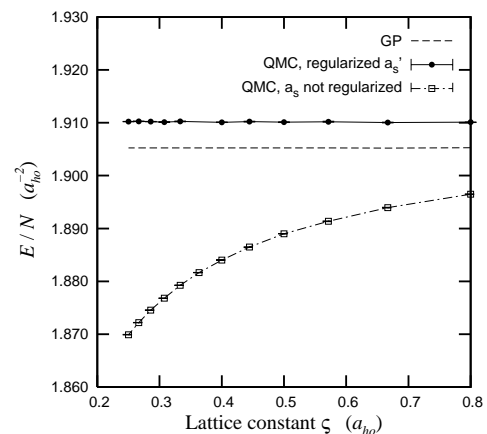


FIG. 7: The effect of finite discretization on the QMC and GP total energies due to the lattice constant  $\varsigma$ . The test system has  $N = 100$ ,  $a_s = 120$  Å. We show the total energy of the system for  $\varsigma$  ranging from  $0.8 a_{ho}$  ( $10 \times 10 \times 10$  lattice) through  $0.25 a_{ho}$  ( $32 \times 32 \times 32$  lattice). Also shown is the QMC energy calculated *without* regularizing the scattering length, which fails to converge. The statistical error bars are smaller than the point size.

On the other hand, the lattice constant is also coupled to the on-site potential that we use, which in turn affects the detailed energetics of the system. The on-site potential effectively has finite range and strength which depend on  $\varsigma$ . This is equiv-

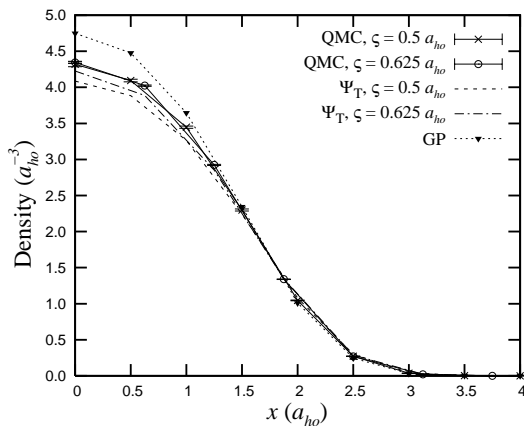


FIG. 8: The effect of finite discretization on the density profiles in QMC and GP. The density profile  $\rho(x, y = 0, z = 0)$  is shown for two different values of the lattice constant,  $\zeta$ . The test system has  $N = 100$  and  $a_s = 400$  Å. The GP curves are indistinguishable. The densities obtained from the QMC trial wave functions are also shown. These are GP-like solutions but with regularized scattering lengths. They do not converge like the QMC or true GP densities.

alent to setting the cutoff momentum  $k_c \propto 1/\zeta$  in the interaction matrix elements. Figure 9 shows the total and kinetic energies as  $\zeta$  is varied. The total energy is less sensitive to the details of the interaction potential, as are the real-space density (see Fig. 8) and the trap energy. The dependence on  $\zeta$  in the kinetic and interaction energies, however, is not negligible. (This dependence is consistent with the observation of Mazziati and co-workers [11] when they varied the range of their soft-sphere repulsive potential.) It is important to note that the nonmonotonic behavior of the kinetic energy is observed at all  $\zeta$  values. As  $\zeta$  is reduced, the upturn is more enhanced, indicating a stronger effect from the interactions as the potential is made narrower and harder.

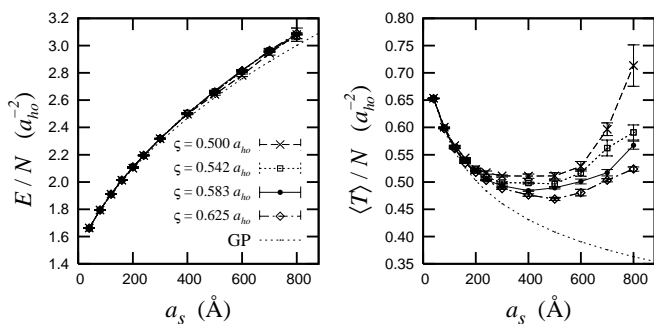


FIG. 9: The effect of the lattice discretization and on-site interaction. The total energy is insensitive to  $\zeta$ , whereas the kinetic energy shows more dependence on the details of the interaction. The system is the same as in Fig. 3.

Ideally, we would like to decouple the basis-size error (due to finite lattice spacing) from the effect of the details of the potential. For this purpose, the on-site pseudopotential is inadequate. The  $\delta$ -function potential is meant to be used with

the short-distance contributions already “integrated out” [40]. The effects above represent corrections from the details of the interaction potential as defined by the on-site form, which change as we vary  $\zeta$ . It is easy to see that in the limit of  $\zeta \rightarrow 0$ , the gas is trivially noninteracting in the exact many-body picture [9], since the range of the interaction potential is zero. However, if the conditions for the validity of the potential are maintained, the corrections should be small and not affect essential properties, as we have illustrated. A better pseudopotential should have an intrinsic decay in momentum space with well-defined convergence properties.

### C. Bias due to phaseless approximation

The phaseless approximation, as demonstrated by the benchmarks in Appendix A, gives an excellent approximation to the true many-body ground state for weak to moderate interaction strengths. Nevertheless, systematic errors on the computed observables are expected. For example, the variational principle, that the total energy computed by QMC is an upper bound to the exact energy, is not guaranteed in the presence of phaseless approximation [27, 28]. We even observe this bias in the  $a_s = 500$  Å results shown in Table II.

The systematic bias is noticeable, but remains quite small up to the largest scattering lengths we study, as can be seen from the benchmark data. It is interesting to compare the phaseless and unconstrained QMC energies in Table II. At a large  $a_s = 500$  Å, the phaseless approximation lowers the kinetic energy (as well as the interaction energy) compared to the unconstrained result. This trend is observed for all  $a_s$  values. Since the phaseless bias increases with the interaction strength, it should lead to an *underestimation* of the upturn of the kinetic energy. Thus the nonmonotonic behavior of the kinetic energy should actually be slightly stronger than shown by QMC.

We have shown in Ref. 22 that the QMC results is independent of the input trial wave function  $\Psi_T$ . This is no longer the case in the presence of the phaseless approximation. The approximation imposes a constraint based on the overlap  $\langle \Psi_T | \phi \rangle$ , and each  $\Psi_T$  in principle has different constraining properties. This dependence is very weak, however, as we observed in our calculations among trial wave functions of the same general form (GP-like).

The phaseless approximation can also affect the Trotter error, which arises from the use of a finite time step  $\Delta\tau$  in Eq. (11). This error is controllable, and can be extrapolated away by running at different values of  $\Delta\tau$ . Because the rotation angle in the random walk is proportional to  $\sqrt{\Delta\tau U}$ , the severity of the phaseless projection is affected by  $\Delta\tau$ , as is the extent of the population fluctuation. The latter is important in back-propagation, where it is highly desirable to keep branching to a minimum. If phaseless projection causes significant loss of the population, the Trotter error will be increased. Procedures that reduce the extent of the phase projection, for example, subtracting the mean-field background shown in Eq. (24), will thus improve computational efficiency (in addition to possibly reducing the systematic error).



## VI. CONCLUSIONS

We have studied the ground state of realistic systems of trapped interacting Bose atomic gases using a many-body auxiliary-field QMC method, as well as GP and the Bogoliubov method under a local density approximation. We observed the effect of correlations in the energetics, condensate fraction, real-space density profiles, and momentum distribution. The density profile is more expanded compared to the GP prediction. The momentum distribution shows enhancement in the occupation of the low- and high-momentum states. The kinetic energy, contrary to the GP estimate, is *not* monotonic with the scattering length  $a_s$ . The Bogoliubov method is able to reproduce this trend qualitatively. Additional calculations on the uniform Bose gas were performed to help understand and quantify our results.

Through this study we also further tested and developed our QMC method. We found that the phaseless approximation developed for electronic systems [27] worked quite well in the context of boson calculations with repulsive calculations. Because of the simplicity of these bosonic systems compared to electronic systems, they have provided an ideal testbed and allowed us to carry out more benchmark calculations and gain additional insights on controlling the phase problem, which is crucial for making QMC more useful for a wide variety of problems. It is hoped that the formalism we developed will allow the study of many interacting Bose, Fermi, and mixed-species systems. The method can also account for different external experiment environments (1-D or 2-D, rotations, anisotropic traps, optical lattices, etc.) quite straightforwardly.

### Acknowledgments

It is a pleasure to thank Markus Holzmann and Henry Krakauer for stimulating discussions. We gratefully acknowledge financial support from NSF and ONR. We also thank the College of William and Mary's Computational Science cluster (SciClone) project and the Center of Piezoelectric by Design for computing support.

### APPENDIX A: BENCHMARK RESULTS ON THE PHASELESS APPROXIMATION IN QMC

In this appendix, we show benchmark results on the phaseless approximation in dealing the complex-phase problem, as discussed in Sec. III A 2. We first show results on a small system for which exact diagonalization can be done. We choose a one-dimensional Bose-Hubbard system. The corresponding Gross-Pitaevskii calculation is also done at the same Hubbard parameters  $t$ ,  $U$ , and  $\kappa$ . (Here  $U$  is a fixed parameter which is the same in QMC and GP.) Table I compares the energetics and condensate fraction obtained using various methods: exact diagonalization, our QMC with the phaseless approximation (ph-QMC), and GP self-consistent projection.

The ph-QMC improves over GP, and in general agrees well with exact diagonalization. The bias due to the phaseless approximation is visible in the trap energy  $\langle \hat{V}_{\text{trap}} \rangle$ . In our phaseless QMC calculation, the mean-field background was subtracted in the Hamiltonian, as shown in Eq. (24). Applying the phaseless approximation directly leads to more population fluctuations in the random walk and larger systematic errors in  $\langle \hat{V}_{\text{trap}} \rangle$  and  $\langle \hat{V}_{2B} \rangle$ .

TABLE I: Benchmark of QMC with the phaseless approximation (ph-QMC) against exact diagonalization. The test system is a 1D Bose-Hubbard Hamiltonian with 13 sites and 4 particles. The parameters are  $t = 2.676$ ,  $U = 1.538$ , and  $\kappa = 0.3503$ . QMC statistical errors are in the last digit, and are shown in parantheses. Error bar in the condensate fraction was not estimated.

Type	$E$	$\langle \hat{T} \rangle$	$\langle \hat{V}_{\text{trap}} \rangle$	$\langle \hat{V}_{2B} \rangle$	$(N_0/N)$
Exact	4.244	1.183	1.793	1.268	98.5%
ph-QMC	4.242(8)	1.182(6)	1.799(1)	1.262(3)	98.4%
GP	4.429	1.029	1.800	1.599	100.0%

We now show calculations on a large system with realistic  $a_s$  values. We use the unconstrained QMC (u-QMC) as the reference. For weak to moderate interaction strength, the unconstrained QMC can be carried out for a short period of time  $\tau$  before the signal is completely lost in large Monte Carlo fluctuations. To obtain the desired accuracy, we perform many short QMC runs and average the results. For each scattering lengths, we verified that the short runs have reached convergence with respect to the projection time. The severity of the phase problem grows rapidly with  $a_s$ , and such runs are not possible for large values of  $a_s$ .

Table II shows the phaseless QMC with the local-energy approximation [Eq. (19)] for 3D trapped gas of 100 atoms with  $a_s = 80 \text{ \AA}$  and  $500 \text{ \AA}$ . The first case represents a typical situation in the trapped atomic gas experiments far from Feshbach resonances, while the second is a medium-strength interaction deep into the range of  $a_s$  we study. The  $\Delta\tau$  parameter was adjusted so that the Trotter error is similar to or smaller than the statistical error. We see that the agreement between the phaseless and unconstrained calculations is good.

As a further check, we compare our QMC result on the uniform Bose gas with an earlier diffusion Monte Carlo (DMC) calculation by Giorgini and co-workers [18], which is exact. We use their results for the soft sphere potential with large radius of  $R = 5a_s$ , which best matches our situation, namely  $\varsigma \sim 2R \sim 10a_s$ . As we show in the left panel of Fig. 10, our results agree well with their DMC energies.

### APPENDIX B: BOGOLIUBOV GROUND STATE

The Bogoliubov approximation for the *homogenous Bose gas* assumes a macroscopic occupancy of the lowest energy state ( $\mathbf{k} = \mathbf{0}$ ), namely  $(N - N_0) \ll N$ . We will work in the thermodynamic limit,  $N \rightarrow \infty$  and  $\Omega \rightarrow \infty$ , keeping the density  $\rho = N/\Omega$  finite. The creation and annihilation

TABLE II: Benchmark of QMC calculations with and without the phaseless constraint for  $a_s = 80 \text{ \AA}$  and  $500 \text{ \AA}$ . We simulate 100 atoms in a 3D harmonic trap with  $a_{\text{ho}} = 8546 \text{ \AA}$ . The simulation lattice is  $24 \times 24 \times 24$ . Shown here are per-particle quantities. All energies are expressed in the unit of  $\hbar\omega_0$ .

Type	$E/N$	$\langle \hat{T} \rangle / N$	$\langle \hat{V}_{\text{trap}} \rangle / N$	$\langle \hat{V}_{2\text{B}} \rangle / N$
$a_s = 80 \text{ \AA}$				
ph-QMC	1.7943(3)	0.5984(3)	0.96029(9)	0.23562(8)
u-QMC	1.7947(2)	0.5987(2)	0.96006(4)	0.23594(4)
GP	1.7924	0.5947	0.95649	0.24121
$a_s = 500 \text{ \AA}$				
ph-QMC	2.6777(2)	0.500(3)	1.5638(6)	0.591(1)
u-QMC	2.6811(4)	0.511(7)	1.563(2)	0.614(3)
GP	2.620	0.408	1.4901	0.721

operators for the zero-momentum state are approximated as scalars,

$$\hat{\phi}^\dagger(\mathbf{0}) \approx \hat{\phi}(\mathbf{0}) \approx \sqrt{N_0}. \quad (\text{B1})$$

We then ignore all terms higher than quadratic in the remaining creation and annihilation operators. The form of the two-body potential also requires that  $ka_s \ll 1$ . Within this approximation, the energy per particle is given by [41]

$$\tilde{E}_{\text{Bog}} \equiv E_{\text{Bog}}/N \quad (\text{B2})$$

$$= \frac{4\pi\rho a_s}{2N} \left[ N - \sum_{\mathbf{k} \neq 0} \left( \alpha_{\mathbf{k}}^2 - \frac{1}{2x_{\mathbf{k}}^2} \right) \right] \quad (\text{B3})$$

$$= 2\pi\rho a_s \left( 1 + \frac{128}{15\sqrt{\pi}} \sqrt{\rho a_s^3} \right), \quad (\text{B4})$$

and the occupation of the  $\mathbf{k}$  momentum state by [42]

$$n_{\text{Bog}}(\mathbf{k}) = \frac{\alpha_{\mathbf{k}}^2}{1 - \alpha_{\mathbf{k}}^2} \quad (\mathbf{k} \neq \mathbf{0}), \quad (\text{B5})$$

where

$$x_{\mathbf{k}} \equiv \frac{|\mathbf{k}|}{(8\pi\rho a_s)^{1/2}} \equiv \xi|\mathbf{k}|, \quad (\text{B6})$$

$$\alpha_{\mathbf{k}} \equiv 1 + x_{\mathbf{k}}^2 - x_{\mathbf{k}} \sqrt{x_{\mathbf{k}}^2 + 2}. \quad (\text{B7})$$

The quantity  $\xi \equiv (8\pi\rho a_s)^{-1/2}$  is the healing length [40] of the condensate. The condensate fraction is given by

$$\frac{N_0}{N} = 1 - \frac{1}{N} \sum_{\mathbf{k} \neq 0} n(\mathbf{k}) \quad (\text{B8})$$

$$= 1 - \frac{8}{3} \sqrt{\frac{\rho a_s^3}{\pi}}. \quad (\text{B9})$$

The kinetic energy per particle can be computed through

$$\tilde{T}_{\text{Bog}} = \frac{1}{2N} \sum_{\mathbf{k} \neq 0} |\mathbf{k}|^2 n(\mathbf{k}). \quad (\text{B10})$$

The summation, however, must be performed with care, as mentioned in Sec. III C. The analytic results for the energy and condensate fraction, Eqs. (B4) and (B9), are obtained by extending the summation variable to infinity, because the contribution from outside the  $ka_s \ll 1$  region is assumed to be small. This assumption does not hold for the kinetic energy, since the sum diverges due to the unphysical nature of  $n(\mathbf{k})$  at large  $|\mathbf{k}|$ .

To benchmark our Bogoliubov approach, we perform QMC and Bogoliubov calculations for a homogenous Bose gas at different scattering lengths, as shown in Fig. 10. We compute the energetics and condensate fraction using three different methods: GP, Bogoliubov, and QMC. As we see here, the first-order Bogoliubov approximation estimates the energetics and condensate fraction very well for a small enough gas parameter (here  $\rho a_s^3 \lesssim 10^{-4}$ ).

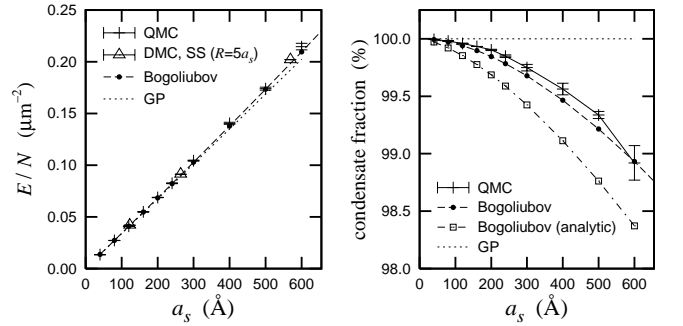


FIG. 10: Benchmark of our QMC and Bogoliubov-LDA calculations in the uniform Bose gas. The system is the same as that in Fig. 4. The upper triangle data points in the g.s. energy plot are from diffusion Monte Carlo (DMC) calculations using a soft sphere (SS) potential [18]. In the condensate fraction plot, we also show the analytic Bogoliubov result without truncation of  $|\mathbf{k}|$ , Eq. (B9).

Note that the condensate fraction estimated by Bogoliubov with the truncation in the sum in  $k$ -space agrees much better with QMC than the analytic Bogoliubov. The analytic Bogoliubov estimate is off, as discussed above, because it is extrapolated to an infinite box size, and it includes contributions from very high momentum states.

We note that the kinetic energy, which is very small in the small  $a_s$  regime, is no longer negligible for larger  $a_s$  values. For  $a_s = 600 \text{ \AA}$ , or equivalently  $\rho a_s^3 = 1.2 \times 10^{-4}$ , the kinetic energy (see Fig. 4) is about 37% of the total energy. This is consistent with our discussion in Sec. IV on the balance between the mean-field and correlation effects.

We can extend the Bogoliubov analysis above to deal with the case of a *inhomogeneous, trapped gas*. We use the so-called local-density approximation (LDA) by treating each lattice site as a locally homogenous gas. The density profile  $\rho(\mathbf{r})$  can be estimated using GP or any other methods which provides a good approximation to the density profile. Using the same  $k$ -space lattice as QMC, we compute the “local” energetics (per particle) and condensate fraction. The density is then used to weight-average the local contributions. The

Bogoliubov-LDA estimate of the kinetic energy is

$$\begin{aligned} \langle \hat{T} \rangle_{\text{Bog-LDA}} = & -\frac{1}{2} \int d^3\mathbf{r} \sqrt{\rho(\mathbf{r})} \nabla^2 \sqrt{\rho(\mathbf{r})} \\ & + \int d^3\mathbf{r} \tilde{T}_{\text{Bog}}[\rho(\mathbf{r})] \rho(\mathbf{r}). \end{aligned} \quad (\text{B11})$$

The interaction energy is given by

$$\langle \hat{V}_{2\text{B}} \rangle_{\text{Bog-LDA}} = \int d^3\mathbf{r} \left( \tilde{E}_{\text{Bog}}[\rho(\mathbf{r})] - \tilde{T}[\rho(\mathbf{r})]_{\text{Bog}} \right) \rho(\mathbf{r}). \quad (\text{B12})$$

The external trap energy is straightforward to compute, namely

$$\langle \hat{V}_{\text{trap}} \rangle_{\text{Bog-LDA}} = \int d^3\mathbf{r} V_{\text{trap}}(\mathbf{r}) \rho(\mathbf{r}). \quad (\text{B13})$$

- 
- [1] M. H. Anderson, J. R. Ensher, M. R. Matthews, C. E. Wieman, and E. A. Cornell, *Science* **269**, 198 (1995).
- [2] S. L. Cornish, N. R. Claussen, J. L. Roberts, E. A. Cornell, and C. E. Wieman, *Phys. Rev. Lett.* **85**, 1795 (2000).
- [3] B. DeMarco and D. S. Jin, *Science* **285**, 1703 (1999).
- [4] F. Schreck, G. Ferrari, K. L. Corwin, J. Cubizolles, L. Khaykovich, M.-O. Mewes, and C. Salomon, *Phys. Rev. A* **64**, 011402 (2001).
- [5] A. G. Truscott, K. E. Strecker, W. I. McAlexander, G. B. Partridge, and R. G. Hulet, *Science* **291**, 2570 (2001).
- [6] E. P. Gross, *Nuovo Cimento* **20**, 454 (1961).
- [7] E. P. Gross, *J. Math. Phys.* **4**, 195 (1963).
- [8] L. P. Pitaevskii, *Sov. Phys.-JETP* **13**, 451 (1961).
- [9] E. Braaten and A. Nieto, *Phys. Rev. B* **56**, 14745 (1997).
- [10] B. D. Esry, *Phys. Rev. A* **55**, 1147 (1997).
- [11] F. Mazzanti, A. Polls, and A. Fabrocini, *Phys. Rev. A* **67**, 063615 (2003).
- [12] S. Fantoni and A. Fabrocini, in *Microscopic Quantum Many-Body Theories and Their Applications*, edited by J. Navarro and A. Polls (Springer-Verlag, Berlin, 1998), Lecture Notes in Physics Vol. 510, p. 119.
- [13] A. Fabrocini and A. Polls, *Phys. Rev. A* **60**, 2319 (1999).
- [14] B. A. McKinney, M. Dunn, and D. K. Watson, *Phys. Rev. A* **69**, 053611 (2004).
- [15] J. L. DuBois and H. R. Glyde, *Phys. Rev. A* **63**, 023602 (2001).
- [16] D. M. Ceperley and B. J. Alder, *Phys. Rev. Lett.* **45**, 566 (1980).
- [17] C. J. Umrigar, M. P. Nightingale, and K. J. Runge, *J. Chem. Phys.* **99**, 2865 (1993).
- [18] S. Giorgini, J. Boronat, and J. Casulleras, *Phys. Rev. A* **60**, 5129 (1999).
- [19] D. Blume and C. H. Greene, *Phys. Rev. A* **63**, 063601 (2001).
- [20] A. R. Sakhel, J. L. DuBois, and H. R. Glyde, *Phys. Rev. A* **66**, 063610 (2002).
- [21] J. L. DuBois and H. R. Glyde, *Phys. Rev. A* **68**, 033602 (2003).
- [22] W. Purwanto and S. Zhang, *Phys. Rev. E* **70**, 056702 (2004).
- [23] N. P. Proukakis, K. Burnett, and H. T. C. Stoof, *Phys. Rev. A* **57**, 1230 (1998).
- [24] B. D. Esry and C. H. Greene, *Phys. Rev. A* **60**, 1451 (1999).
- [25] Y. Castin, *J. Phys. IV France* **116**, 89 (2004), also available at <http://arXiv.org/abs/cond-mat/0407118>.
- [26] S. Zhang, J. Carlson, and J. E. Gubernatis, *Phys. Rev. B* **55**, 7464 (1997).
- [27] S. Zhang and H. Krakauer, *Phys. Rev. Lett.* **90**, 136401 (2003).
- [28] J. Carlson, J. E. Gubernatis, G. Ortiz, and S. Zhang, *Phys. Rev. B* **59**, 12788 (1999).
- [29] N. N. Bogoliubov, *J. Phys. (U.S.S.R.)* **11**, 23 (1947).
- [30] T. D. Lee, K. Huang, and C. N. Yang, *Phys. Rev.* **106**, 1135 (1957).
- [31] T. T. Wu, *Phys. Rev.* **115**, 1390 (1959).
- [32] W. Kohn, *Rev. Mod. Phys.* **71**, 1253 (1999).
- [33] M. R. Andrews, M.-O. Mewes, N. J. van Druten, D. S. Durfee, D. M. Kurn, and W. Ketterle, *Science* **273**, 84 (1996).
- [34] M. R. Andrews, D. M. Kurn, H.-J. Miesner, D. S. Durfee, C. G. Townsend, S. Inouye, and W. Ketterle, *Phys. Rev. Lett.* **79**, 553 (1997).
- [35] L. V. Hau, B. D. Busch, C. Liu, Z. Dutton, M. M. Burns, and J. A. Golovchenko, *Phys. Rev. A* **58**, R54 (1998).
- [36] A. Fabrocini and A. Polls, *Phys. Rev. A* **64**, 63610 (2001).
- [37] G. S. Nunes, *J. Phys. B: At. Mol. Opt. Phys.* **32**, 4293 (1999).
- [38] A. Banerjee and M. P. Singh, *Phys. Rev. A* **64**, 63604 (2001).
- [39] H. Fu, Y. Wang, and B. Gao, *Phys. Rev. A* **67**, 053612 (2003).
- [40] A. J. Leggett, *Rev. Mod. Phys.* **73**, 307 (2001).
- [41] K. Huang, *Statistical Mechanics* (John Wiley & Sons, New York, 1987), 2nd ed.
- [42] The continuum momentum distribution, which is often referred to in the main text, *per particle*, is given by  $\pi(\mathbf{k})/N \equiv \tilde{\pi}(\mathbf{k}) = n(\mathbf{k})/[(2\pi)^3 \rho]$ .